

Chirality-Assisted High-Efficiency Metasurfaces with Independent Control of Phase, Amplitude, and Polarization

He-Xiu Xu,* Guangwei Hu, Lei Han, Menghua Jiang, Yongjun Huang, Ying Li, Xinmi Yang, Xiaohui Ling, Liezun Chen, Jianlin Zhao, and Cheng-Wei Qiu*

Simultaneously independent control of phase, amplitude, and polarization is pivotal yet challenging for manipulating electromagnetic waves by transmissive metasurfaces. Huygens' metasurface affords a high-efficiency recipe primarily by engineering phase-only meta-atoms, restricting itself from realizing unprecedentedly complex functions of the transmission beam. Here, a 3D chirality-assisted metasurface concept relying on integrated magnetoelectric meta-atoms is proposed. It empowers the completely decoupled and arbitrary control of phase and amplitude at large incident angles and arbitrary polarizations. This strategy thus facilitates very sophisticated beam manipulations at close-to-unity cross-polarized efficiency via trilayer integrated resonators with mutual twist. The prescribed phase coverage can be determined by geometrical footprints of the unit cell, while the global azimuthal twist unlocks the capability of tuning amplitudes without affecting the phase. The concept and significance of it are validated to implement several proof-of-prototype demanding functionalities by thin metasurfaces of $\lambda_0/12$, which generate self-accelerating diffraction-free Airy beams, lateral and axial dual focusing, and even specific multiplexed beam shaping, respectively. This finding opens up an alternative way in very fine control of light with minimalist complexity and advanced performance. It can stimulate novel and high-performance versatile photonic metadevices, thanks to the fully independent control of phase, amplitude, and polarization.

1. Introduction

The explosive field of metasurface has intrigued a huge interest from both physics and engineering communities due to its exotic behaviors and promising applications. It, composed of a mass of subwavelength-spaced meta-atoms, has afforded extraordinary capabilities to manipulate electromagnetic (EM) waves.^[1–39] The local amplitude, phase, and polarization are three important characteristics for output EM wavefront control, and previous pursuing of light manipulation via metasurfaces could be generally subjected into processing one or two of them. However, the simultaneous modulation of the above three items is rarely reported. In recent years, we have witnessed some progress toward the simultaneous amplitude and phase control.^[14–23] Therein, superior performances or completely new functionalities are realized such as higher-order diffractions,^[14] quality-enhanced hologram,^[16] and radar cross section reduction.^[21] However, most attempts are either in reflection geometry,^[19–21] or with

Prof. H.-X. Xu
Air and Missile Defense College
Air Force Engineering University
Xi'an 710051, China
E-mail: hxxuellen@gmail.com


Prof. H.-X. Xu, Dr. G. Hu, Dr. L. Han, M. Jiang, Y. Li, Prof. C.-W. Qiu
Department of Electrical and Computer Engineering
National University of Singapore
Singapore 117583, Singapore
E-mail: eleqc@nus.edu.sg

Prof. H.-X. Xu, X. Ling, L. Chen
Hunan Provincial Key Laboratory of Intelligent Information
Processing and Applications
College of Physics and Electronic Engineering
Hengyang Normal University
Hengyang 421002, China

Dr. L. Han, Prof. J. Zhao
School of Natural and Applied Sciences
Northwestern Polytechnical University
Xi'an 710072, China

Prof. Y. Huang
School of Information and Communication Engineering
University of Electronic Science and Technology of China
Chengdu 611731, China

Prof. X. Yang
School of Electronics and Information Engineering
Soochow University
Suzhou 215006, China

 The ORCID identification number(s) for the author(s) of this article can be found under <https://doi.org/10.1002/adom.201801479>.

DOI: 10.1002/adom.201801479

extreme angle sensitivity and low efficiency whose maximum is fundamentally restricted by 25%^[14–18] which may seriously hinder the real-world applications. The exclusive work for high-efficiency amplitude–phase control was realized using Huygens' metasurfaces. However, the simultaneous electric and magnetic responses through double-layer vias may complicate the design. Moreover, all these designs rendered the polarization control totally irrelevant or essentially unaddressed. Most recently, propagation phase was combined with the geometric phase (hybrid approach) to engineer complete phase and polarization control.^[24–26] The extra degree of freedom (DOF) can be utilized to break the locked reverse phase profile under two helicities of circularly polarized wave. Other different multifunctionalities are realized at different polarization states by combining the above dual DOFs.^[27–29]

On the other hand, much attention has been paid to enhance the efficiency which is critically important for photonic devices. To date, different approaches were proposed to circumvent it in both reflection and transmission geometries,^[30–39] for example, by using active phase compensation,^[30] satisfying certain phase criterion,^[31–33] incorporating both electric and magnetic responses,^[34–36] low-loss all-dielectric metasurfaces,^[38,39] etc. However, these designs are confined to phase- or polarization-only modulation, making the kaleidoscopic wavefront control particularly challenging. Moreover, the dielectric metasurfaces typically require the thickness comparable to the wavelength and thus is conflicting with the increasing demand for integrated optics.

Here, we propose a scheme that is capable of complete and decoupled amplitude, phase, and polarization modulation with high efficiency in transmission geometry, advancing a step beyond what is achievable by available metasurfaces.^[14–23] The distinguished underlying principle is to merge local 3D layered cross-coupling, and global parametric and orientation tuning to facilitate additional full polarization control and fascinating angle-insensitive feature. By introducing a set of vertically coupled modes, a total cross-polarization conversion with near 100% transmission is actualized within a moderate bandwidth. Most importantly, the transmission amplitude can be continuously tuned by altering the orientation angle without affecting the local phase at arbitrary polarization. Such exotic merit allows full decoupling of phase and magnitude which can be engineered for kaleidoscopic wavefront shaping. To verify the concept, the demanding Airy packet with long nondiffracting parabolic trajectories and bifocusing metalens without interleaving are realized in microwave regime. Moreover, the significance of it has been demonstrated by possible applications in specific multiplexed beam shaping. Our approach could open up new avenues for arbitrary high-performance kaleidoscopic wavefront shaping with unprecedented DOF.

2. Principle and Properties of the Anisotropic Meta-Atom

To completely remove the metasurface-imparted correlation between phase, amplitude, and polarization, we propose a chirality-assisted scheme by introducing integrated interlayer resonators. Therein, full cross-polarization conversion (t_{xy})

can be engineered with residual three components (r_{xy} , r_{yy} , and t_{yy}) completely suppressed, facilitating a near 100% transmission, as shown in the left panel of **Figure 1a**. Most importantly, such chirality scheme as rigorously demonstrated below assists inherent phase–amplitude decoupling for output cross-polarization components. Therefore, our scheme resolves both the issues of the inefficient phase–amplitude decoupling of copolarized transmissive Huygens' metasurfaces, and angle-sensitive low-efficiency cross-polarized metasurfaces (which is fundamentally limited below 25% owing to the symmetry requirement).

To realize complete cross-polarization conversion immune to large incidence angles, the subwavelength meta-atom should exhibit 3D chiral architectures^[40] and strong local chirality without any mirror or rotation symmetry. Such structural chirality yields strong cross-coupling between electric and magnetic fields at resonances. Having these aspects in mind, the basic building block for complete decoupling of amplitude, phase, and polarization is designed and shown in the inset of **Figure 1a**. It is an interesting analog to the mechanical counterpart of three-gear systems, as shown in the right panel of **Figure 1a**. The traditional dilemma is that the tuning of either party (phase, amplitude, or polarization) will automatically affect the rest. This will lock up the metasurface functions and thereby limit its potentials. Now, our concept can unlock and separate those three “gears” such that each party could be independently tuned, which provides unprecedented access to the flatland of high-efficiency metasurfaces.

The transmissive meta-atom consists of stacked triple-layer twisted split ring resonators (SRRs) sandwiched by two dielectric spacer layers with a dielectric constant (ϵ_r) of 4.5 and a thickness (h) of 1.5 mm. Each pair of neighboring SRRs has a mutual twist angle of $\Phi = 45^\circ$. Such judicious choice, as discussed below, offers resonance hybridization and interlayer magnetoelectric cross-coupling, which are the key for near-unitary polarization transformation. By shining the composite meta-atom from the bottom with y -polarized plane wave, triple resonant modes can be coherently excited, manifesting three near-unity resonant peaks across the $|t_{xy}|$ spectrum (**Figure 1b** and **Figure S1** (Supporting Information)), and totally suppressed respective dips across the $|t_{yy}|$ or $|t_{xx}|$ spectrum (**Figure S2a**, Supporting Information). These modes can be identified from the field/current distributions shown in the inset of **Figure S2a** (Supporting Information) from low to high frequencies. They correspond orderly to the symmetric dipolar-resonant (I), hybrid (II), and asymmetric (III) LC-resonant modes of three SRRs with $\Phi = 0^\circ$ (SRR₁), 45° (SRR₂), and 90° (SRR₃), respectively, and are very robust against the dielectric thickness, as shown in **Figure 1b**. In addition to the broadband transmission window, the superposition of these chirality-assisted resonant modes also enhances the discontinuous phase coverage without affecting the constant transmission amplitude. The Δ parameter $\Delta = |t_{xy}|^2 - |t_{yx}|^2$ of asymmetric transmission is more than 0.6 across a fractional bandwidth of 32.1%, revealing a broadband giant chirality.

By coherently varying the radius (R) of the above triple SRRs, desirable full 2π phase cover of t_{xy} (denoted as φ) is engineered within the transmission window (**Figure 1c**

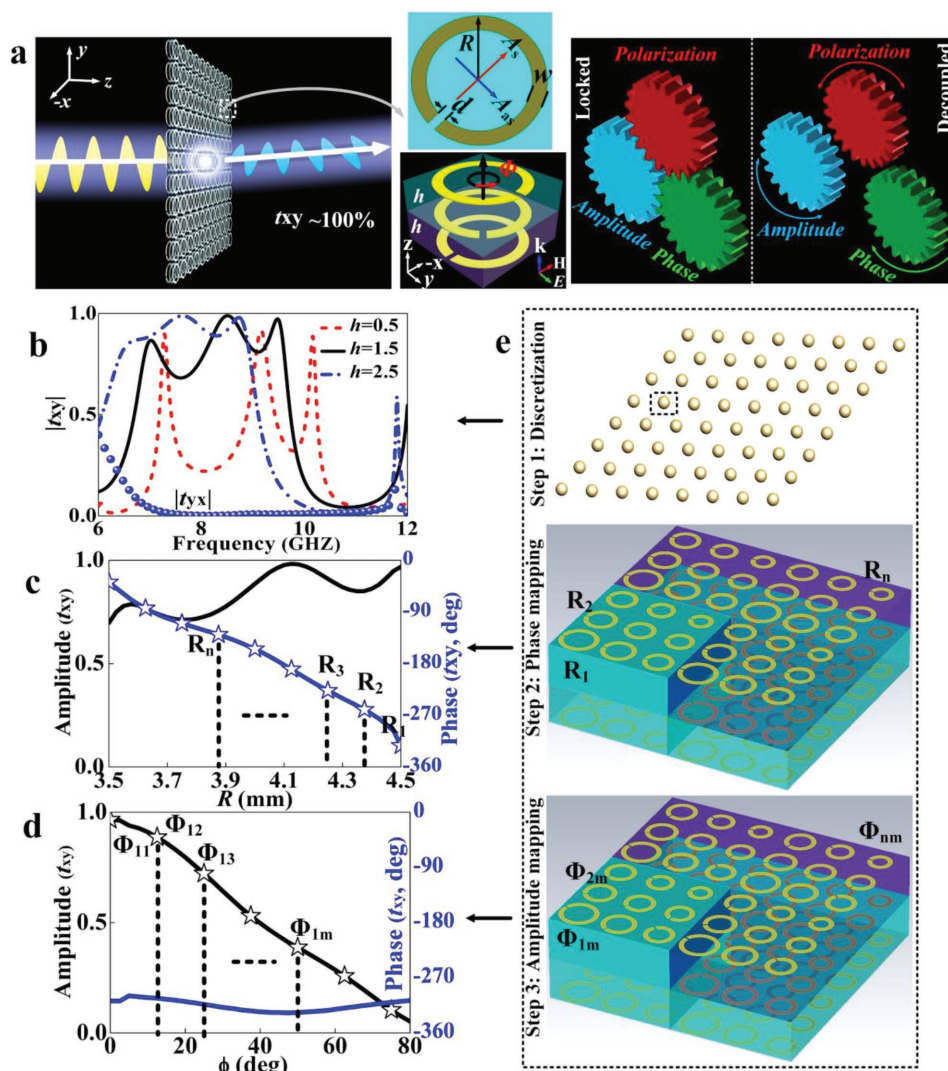


Figure 1. Conceptual illustration and characterization of the proposed transmissive triple-layer meta-atom with high-efficiency cross-polarization conversion. a) Schematic illustration of the metasurface. The left (the topology of the basic meta-atom shown in the inset) and right panel represents a system with high-efficiency cross-polarization transmission, and completely independent control of phase, amplitude, and polarization in the analog of mechanical trigear systems, respectively. b) FDTD-calculated cross-polarization transmission spectrum. FDTD-calculated transmission amplitude and phase responses of t_{xy} as a function of c) ring radius R ($\Phi = 0^\circ$) and d) orientation angle Φ ($R = 4.5$ mm) at 9.45 GHz. e) Illustration of the three-step design process. All meta-atoms are with $d = 0.6$ and a square lattice constant of 10×10 mm². Here, the width of SRRs $w = 1$ mm is kept constant for the simplicity of design.

and Figure S2b (Supporting Information)). Although slight fluctuations manifest in $|t_{xy}|$, the transmission of $|t_{xy}| > 0.7$ fulfills satisfactory requirements for wavefront control since the dependence of performances on unitary amplitude in amplitude–phase metasurface has been significantly relaxed compared to that in phase-only case. More flat transmissions with shallower dips can be engineered by using a thicker dielectric board, which poses slight penalty on the vertical profile. More importantly, continuous amplitude variation is achieved from unity to zero by tuning the orientation angle Φ of SRRs without affecting the phase response in transmission window, as shown in Figure 1d and Figures S1 and S2c (Supporting Information). Such merit can find critical applications in synthesis of complex wave fields, novel beam shaping, and high-quality holographic

images. Although a phase fluctuation of 22° and 5° is inspected for the meta-atom of $R = 4.5$ and $R = 3.8$ mm, respectively, even the maximum level of 22° under the strongest interelement mutual coupling ($R = 4.5$ mm) still poses negligible penalty to the prescribed functions. Such a Φ -immune response facilitates extreme flexibility in reshaping wavefront through individually altering the orientation angles and structure parameters. Moreover, our strategy although made of stacked SRRs, is very thin with a vertical profile of only $\lambda_0/12$, which could be very suitable and essential for integrated flat photonic devices. The phase of t_{xy} as a function of R (ϕ – R relation) can be obtained based on finite-difference time-domain (FDTD) simulations. Intriguingly, we find below that the amplitude of t_{xy} can be derived analytically as a function of Φ .

The analytical derivation starts with the symmetric and antisymmetric mode analyses of a single-layer SRRs with open split directed toward Φ relative to the x -axis. For normally incident x -polarized plane wave, symmetric ($E_s^{\text{out}} = E_x^{\text{in}} \cos \Phi A_s e^{i\varphi_s}$) and antisymmetric ($E_{as}^{\text{out}} = E_x^{\text{in}} \sin \Phi A_{as} e^{i\varphi_{as}}$) modes are simultaneously excited and are decoupled into x - and y -polarized components as

$$\begin{aligned} E_x^{\text{out}} &= E_x^{\text{in}} A_s e^{i\varphi_s} \cos \Phi \cos \Phi + E_x^{\text{in}} A_{as} e^{i\varphi_{as}} \sin \Phi \sin \Phi \\ &= E_x^{\text{in}} (A_s e^{i\varphi_s} \cos^2 \Phi + A_{as} e^{i\varphi_{as}} \sin^2 \Phi) \end{aligned} \quad (1)$$

$$\begin{aligned} E_y^{\text{out}} &= E_x^{\text{in}} A_s e^{i\varphi_s} \cos \Phi \sin \Phi + E_x^{\text{in}} A_{as} e^{i\varphi_{as}} \sin \Phi \cos \Phi \\ &= \frac{1}{2} E_x^{\text{in}} \sin 2\Phi (A_s e^{i\varphi_s} - A_{as} e^{i\varphi_{as}}) \end{aligned} \quad (2)$$

Similarly, the output x - and y -polarized components under normally incident y -polarized plane wave can be expressed as

$$\begin{aligned} E_x^{\text{out}} &= E_y^{\text{in}} A_s e^{i\varphi_s} \sin \Phi \cos \Phi + E_y^{\text{in}} A_{as} e^{i\varphi_{as}} \cos \Phi \sin \Phi \\ &= \frac{1}{2} E_y^{\text{in}} \sin 2\Phi (A_s e^{i\varphi_s} - A_{as} e^{i\varphi_{as}}) \end{aligned} \quad (3)$$

$$\begin{aligned} E_y^{\text{out}} &= E_y^{\text{in}} A_s e^{i\varphi_s} \sin \Phi \sin \Phi + E_y^{\text{in}} A_{as} e^{i\varphi_{as}} \cos \Phi \cos \Phi \\ &= E_y^{\text{in}} (A_s e^{i\varphi_s} \sin^2 \Phi + A_{as} e^{i\varphi_{as}} \cos^2 \Phi) \end{aligned} \quad (4)$$

By taking Φ as $\Phi = 0^\circ$, 45° , and 90° , we immediately obtain the output components for the three individual single-layer SRRs. Then, the output components for the whole bottom-to-top SRRs can be derived by cascading these transmission matrixes and taking the outputs of the former SRRs as new inputs of the latter SRRs. After trivial yet straightforward derivation (Section S1, Supporting Information), we eventually obtain the output x - and y -polarized components of the triple-layer meta-atom under x -polarization as

$$E_y^{\text{out}} = \frac{1}{8} E_x^{\text{in}} A [\cos 2\Phi (A^2 + B^2) + 2AB] \quad (5)$$

$$E_x^{\text{out}} = \frac{1}{8} E_x^{\text{in}} [-(AB^2 + A^3) \sin 2\Phi + B^3 - A^2 B] \quad (6)$$

Here, $\alpha = A_s e^{i\varphi_s}$, $\beta = A_{as} e^{i\varphi_{as}}$, $A = \alpha - \beta$, and $B = \alpha + \beta$. Based on the same procedure, the x - and y -polarized outputs under y -polarized excitation are formulized as

$$E_y^{\text{out}} = \frac{1}{8} E_y^{\text{in}} [(B^2 - A^2)B - (B^2 A - A^3) \sin 2\Phi - 2A^3 \sin^3 2\Phi] \quad (7)$$

$$E_x^{\text{out}} = \frac{1}{8} E_y^{\text{in}} A [-2AB - 2A^2 \cos^3 2\Phi + (3A^2 + B^2) \cos 2\Phi] \quad (8)$$

Equations (5)–(8) illustrate that only the cross-polarization components take the pure cosine term which implies a continuous decreasing of the amplitude from the maximum to the minimum. This is the key for independent amplitude control and interprets why Huygens' metasurfaces cease to perform this task because the simultaneous electric and magnetic

responses for copolarization transmission inherently limits the capability of phase–amplitude decoupling.

The above analytical prediction has been verified by satisfactory agreement of output t_{xy} between the theoretically calculated and FDTD-simulated results of the triple-layer meta-atom with $R = 4.5$ nm, as shown in Figure S2d (Supporting Information). A Φ -immune flat phase response and a Φ -dependent monotonically decreasing amplitude response are clearly appreciated. Therefore, Equations (7) and (8) indirectly predict that the transmission phase and magnitude could be separately controlled since engineering individual phase modulation with quasi-constant magnitude by exclusively changing the structural parameters (radius R) is intuitive. The analytical t – Φ relation offers us a quick way to determine the rotation angles of each meta-atom according to prescribed transmission amplitudes and thus avoids time-consuming parametric analyses in metadvice design by reducing the calculation complexity from $n \times m$ to n . With the above feature of our meta-atom, the design of metasurface with m -level amplitude and n -level phase distribution for prescribed functionality is simple and straightforward, which typically involves three steps (Figure 1e). First, determine the required amplitude and phase distributions at the operation frequency f_0 . Second, determine R_n of each meta-atom by phase mapping according to the target phase profile and φ – R relation (Figure 1c and Figure S2b (Supporting Information)). Third, finalize the design (amplitude mapping) through spatially rotating each meta-atom with Φ_{nm} following the destined amplitude profile and analytical t – Φ relation (Figure 1d).

3. Generation of Finite-Energy Airy Beams

The exotic feature of complete yet decoupled polarization, amplitude, and phase modulation can be engineered for fine and arbitrary extreme-demanding beam manipulation. To verify this concept, here we first design and characterize a metadvice that is capable of generating Airy wave packets^[18,41–43] with unique self-bending and self-healing properties in the absence of any external potential. The decoupling of fixed relationship between phase and amplitude is the key for engineering such purpose. For arbitrary ballistic trajectory of 1D finite-energy Airy beam, the propagation dynamics evolve according to Airy dispersionless solution of the paraxial diffraction equation^[43]

$$\begin{aligned} \phi(s, \xi) &= \text{Ai}(s - (\xi/2)^2 + ia\xi) \exp(as - (a\xi^2/2) - i(\xi^3/12)) \\ &\quad + i(a^2 \xi/2) + i(s\xi/2) \end{aligned} \quad (9)$$

Here, $\xi = z/kx_0^2$ is the normalized propagation length, $s = x/x_0$ is the dimensionless transverse scale, a is the truncation factor (small positive variable) to guarantee infinite Airy tail, and k is the free-space wave vector. From Equation (9), the required amplitude and phase distributions across the metasurface aperture can be immediately obtained as $\phi(s, 0) = \text{Ai}(s) \exp(as)$ due to its nondiffraction feature. Such 1D Airy beam can be readily extended to 2D case with amplitude and phase profiles of $\phi(x, y, 0) = \text{Ai}(x/x_0) \text{Ai}(y/y_0) \exp[ax/x_0 + ay/y_0]$, which can be verified by taking it into the 2D normalized paraxial diffraction equation (analog to free-potential Schrödinger

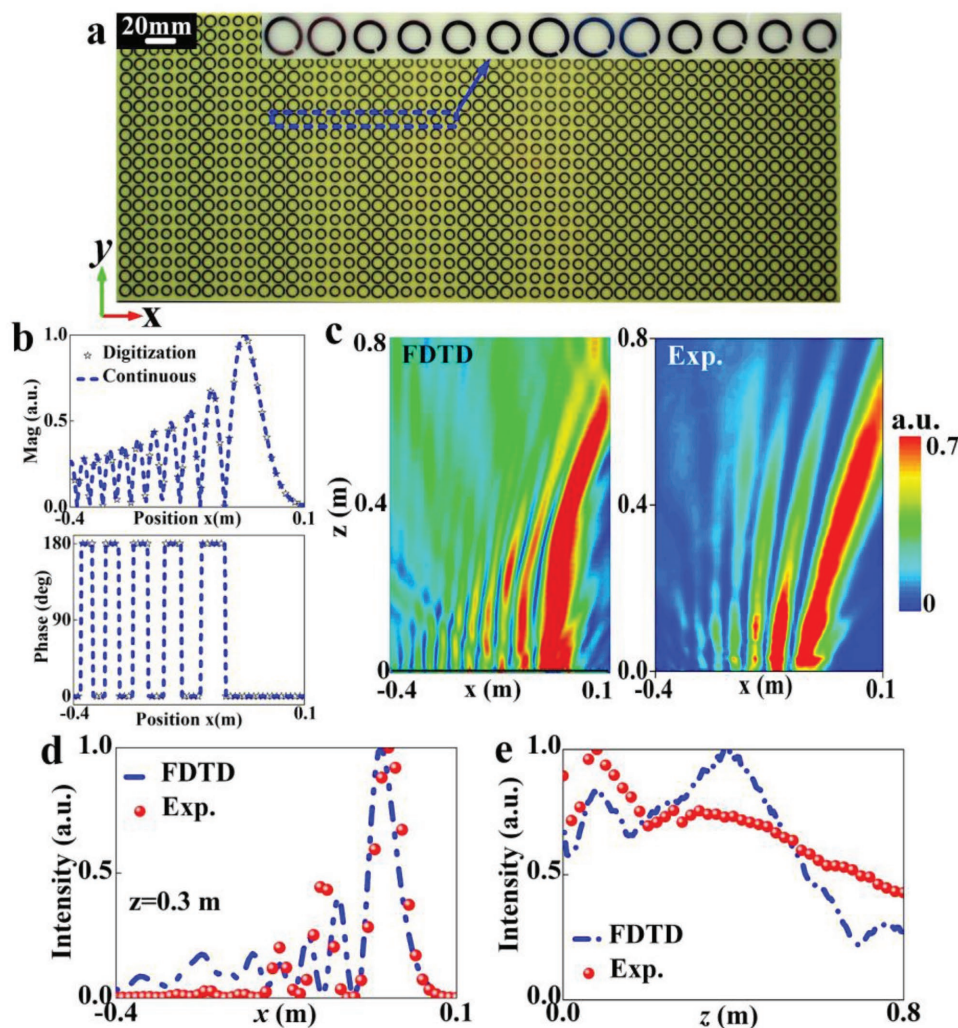


Figure 2. Numerical and experimental characterization of the propagation dynamics of the designed finite-energy Airy packet. a) Photograph of the fabricated sample with $M \times N = 51 \times 20$ pixels (top view). b) Required (blue dashed) and digitized (pentacle) amplitudes (top) and phases (bottom) of the designed Airy packet. c) FDTD-calculated (left) and experimentally measured (right) E-field (E_x) distributions in the xz -plane at 9.4 GHz. Comparison of intensity cross-section E_x^2 d) at $z = 0.3$ m and e) along the propagation of the main beam at 9.4 GHz.

equation). In actual realization, the full amplitude and phase distributions across the metasurface are discretized by the lattice constant (10 mm) of our high-efficiency meta-atoms.

For generality, we engineered three individual designs for both 1D and 2D Airy functions with identical parameters of $a = 0.06$ and $x_0 = 0.03$ in all cases and performed both theoretical and full-wave FDTD numerical simulations to examine their exotic features (Figures S2–S5, Supporting Information). In 1D case, two metastrips with a total of $M \times N = 31 \times 1$ and 51×1 meta-atoms are considered (structures only varied along the x -direction by imposing periodic boundary conditions along the y -direction), whereas in 2D case, a sum of $M \times N = 31 \times 31$ pixels are utilized with equal scale in the x - and y -directions by assigning open boundary conditions along its four bounds. For experimental verification, we actualize the second design by fabricating a metasurface (Figure 2a) composed of $M \times N = 51 \times 20$ pixels through precisely imparting the amplitude and $(0, \pi)$ phase-jump profile shown in Figure 2b over the aperture.

Two basic meta-atoms with $R = 4.5$ and 3.8 mm are utilized to implement the two jump phases. In FDTD and experimental characterizations, these metasurfaces are illuminated by y -polarized plane wave with the output E_x components recorded through near-field mapping measurement system in a microwave anechoic chamber (experimental setup detailed in Figure S11 in the Supporting Information).

Figure 2c shows the recorded E_x distributions in the xz -plane by scanning an area of $0.5 \text{ m} \times 0.8 \text{ m}$ with a step resolution of 10 mm (Experimental Section) at $f_0 = 9.4$ GHz. Evidently, numerical results are consistent with the measured ones. The parabolic trajectories and invariant E_x intensity as its original are clearly observed even after long propagation, implying self-accelerating character and desirable diffraction-free propagation of the Airy wave packet. Similar cross-section of E-field intensity can be observed within a wide range of frequencies of 8.4–9.8 GHz, as shown in Figures S4b and S6 (Supporting Information), indicating a satisfactory operation bandwidth.

Figure 2d,e further shows the E_x intensity curve at $z = 0.3$ m and along the z -direction for quantitative analyses. Consistent numerical and experimental results indicate an obvious oscillatory and exponentially decaying feature of the Airy function from the main lobe and side lobes (different oscillatory periods). The desirable nondiffracting propagation characterized by the full width at half maximum (FWHM) of the main lobe is 0.7 m (0.6 m in FDTD simulation) before the main lobe gradually fades out. Moreover, we also find that the Airy packet starts to deteriorate first from the tail and then to the mainbeam as frequency goes beyond f_0 . The slight discrepancies especially for the fluctuations of intensity along propagating direction are attributable to the tolerances inherent in fabrications and measurements. The measured fractional bandwidth characterized by diffraction-free propagation distance larger than 0.64 m is about 11.1% (8.5–9.5 GHz). Such exotic feature may find various applications in wireless communications, optical micromanipulation, optical bullet, and producing curved plasma channels. Similar diffraction-free propagation and self-accelerating character of the Airy function can be seen from theoretical and FDTD results of other two designs in Figures S2, S3, and S5 (Supporting Information).

4. Bifocal Metalens with Lateral or Axial Alignment of Two Foci

Next, we proceed to demonstrate another applications of our flexible metasurface by designing two bifocal metalenses with lateral or axial alignment of two foci. We show that in principle, arbitrary and decoupled bifocal positions can be easily implemented, which more importantly does not require the spin manipulation. For these tasks, the required phase and amplitude profiles across the aperture should fulfill the following conditions.

$$\sigma(x, \lambda) = \alpha_1 e^{j \frac{2\pi}{\lambda} (\sqrt{(x-d/2)^2 + F^2} - F)} + \alpha_2 e^{j \frac{2\pi}{\lambda} (\sqrt{(x+d/2)^2 + F^2} - F)} \quad (10a)$$

$$\sigma(x, \lambda) = \alpha_1 e^{j \frac{2\pi}{\lambda} (\sqrt{x^2 + F_1^2} - F_1)} + \alpha_2 e^{j \frac{2\pi}{\lambda} (\sqrt{x^2 + F_2^2} - F_2)} \quad (10b)$$

Here, λ is the designed wavelength at $f_0 = 9.5$ GHz, α_1 and α_2 are the strength of the two foci, $F = 150$ mm is the focal point of two foci of the first metalens with lateral distance of $d = 60$ mm, whereas $F_1 = 55$ and $F_2 = 130$ mm are two axial focal points of the second metalens. Both the lenses are targeted at 9.5 GHz with $\alpha_1 = \alpha_2 = 0.5$. The continuous amplitude and phase patterns required for metalens design in both 1D and 2D case are achieved by performing theoretical calculations (Figure S8d,e, Supporting Information). In both full-wave FDTD simulations and experiments, we illuminate the metalens with normally incident y -polarized plane wave along the z -direction and record the scattered x -polarized radiation.

Figure 3 plots the fabricated photograph of the first metalens composed of $M \times N = 31 \times 25$ pixels with spatially varied structures and orientations, and exotic properties exhibiting dual lateral foci. We utilize six-level (pentacle) phase modulation to digitize the required full profiles (dashed) of the 1D metalens

(Figure 3a). More design details for each pixel can be found in Table S1 (Supporting Information). Each level corresponds to a meta-atom with specific radius and orientations (Figure 3b), which are determined based on the criterion of minimum amplitude tolerances. By doing so, consistent amplitude and phase profiles can be appreciated between continuous and digitization values. Figure 3c shows FDTD-simulated E_x map, while Figure 3d depicts the measured 2D contour of the near-field E_x distribution by scanning an area of 180×90 mm² in steps of 5 mm. All fields are normalized to their global maximum. As expected, two focal spots with extremely localized intensity and a distance of $d = 59$ mm along the x -direction are observed near $z = 150$ mm at 9.5 GHz, indicating prescribed dual focusing behavior with lateral alignment of two foci predicted by theoretical results of 1D and 2D metalenses (Figure S8c,e, Supporting Information). The bifurcated two beams resemble two individual EM waves emitted from two emerging sources. The dual-focusing capability at other frequencies can be observed in Figures S8f and S9 (Supporting Information). As shown in Figure 3e, good agreement is observed between numerical and experimental E_x along $z = 150$ mm, indicating a measured FWHM beamwidth of 20 and 21 mm ($0.63\lambda_0$) for the two foci at 9.5 GHz. The nonideal alignment of metalens and feeding horn gives rise to the slight distortion of fields, especially for the oblique manifestation of the two foci. Nevertheless, this poses little effect on identifying the high-resolution dual focusing behavior.

Figure 4 shows the properties of bifocal metalens with axial alignment of two foci. As can be seen from Figure 4a,c, one-fold and twofold symmetric amplitude and phase patterns are clearly observed for the 1D and 2D axial bifocal metalens. For verification, we designed the 1D metalens by using nine-level (pentacle) phase modulations (Table S2, Supporting Information) to cautiously digitize the required full 1D phase profile (dashed) depicted in Figure 4a. Then, the metalens layout is figured out by following the design procedure derived above. As expected, both theoretical (Figure 4b,d) and FDTD (Figure 4e–g) results agree well, implying desirable dual focusing behavior from the two localized spots with the maximum intensity along the optical axis (z -axis). The axial focusing property is observed almost the same for the 1D and 2D metalens except for the non-focusing uniform intensity and strongly localized spot intensity observed along the y -direction. Note that the slightly different focal intensity at the two foci are probably induced by inherently different focusing capability of finite-size lens at different axial positions. Some deviations observed in FDTD calculations are probably induced by the phase/amplitude discrepancy between the finally utilized meta-atoms and the ideal ones.

5. Specific Multiplexed Beam Shaping

Last but not the least, our chirality-assisted metasurfaces with independent amplitude–phase control can find many other interesting applications in practice, which will be briefly introduced in this section. Here, we propose to utilize such a concept to synthesize arbitrary multiplexed shaping patterns with prescribed gain and coverage for spacecraft, air traffic control radars, and wireless communications. Therein, we can

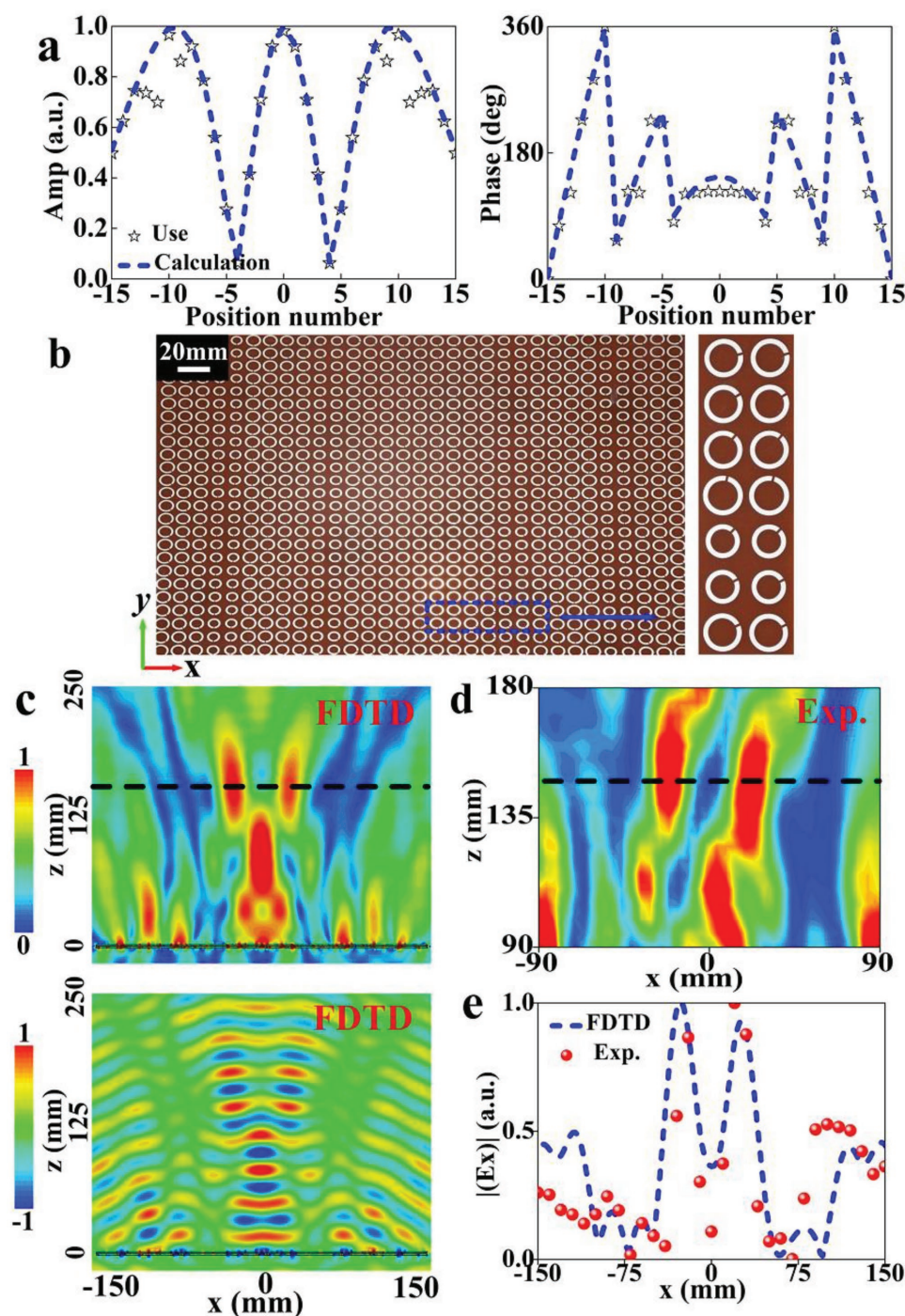


Figure 3. Design and characterization of the 1D bifocal metalens with lateral alignment of two foci. a) Required (blue dashed) and digitized (pentacle) normalized amplitudes (left) and phases (right) of the designed lateral bifocal metalens in 1D case. b) Photograph of the fabricated sample with a total of $M \times N = 31 \times 25$ pixels (top view). c) FDTD-simulated and d) experimentally measured E-field (E_x) distributions at 9.5 GHz. The top panel of (c) shows the $|E_x|$, while the bottom panel plots the $\text{Real}(E_x)$. e) Comparison of simulated and measured E_x intensity along the line $z = 150$ mm at 9.5 GHz.

synthesize a set of specific shaped beam patterns with continuously changed radiation/scattered performances based on sophisticated optimization method. To approve this proposal, we have designed three metasurfaces exhibiting flat-top beams of different coverage of 35° , 55° , and 75° in elevation and a low sidelobe below -20 dB, as shown in Figure 5a. Such a target is

accomplished by incorporating different amplitude and phase profiles shown in Figure 5b,c based on genetic algorithms. After ≈ 2000 iterations (Figure 5d), the cost function reaches a stable value (converged) with prescribed convincing pattern bounds in the shaped region. Accompanied by available mechanically or electrically reconfigurable techniques, these coherent functions

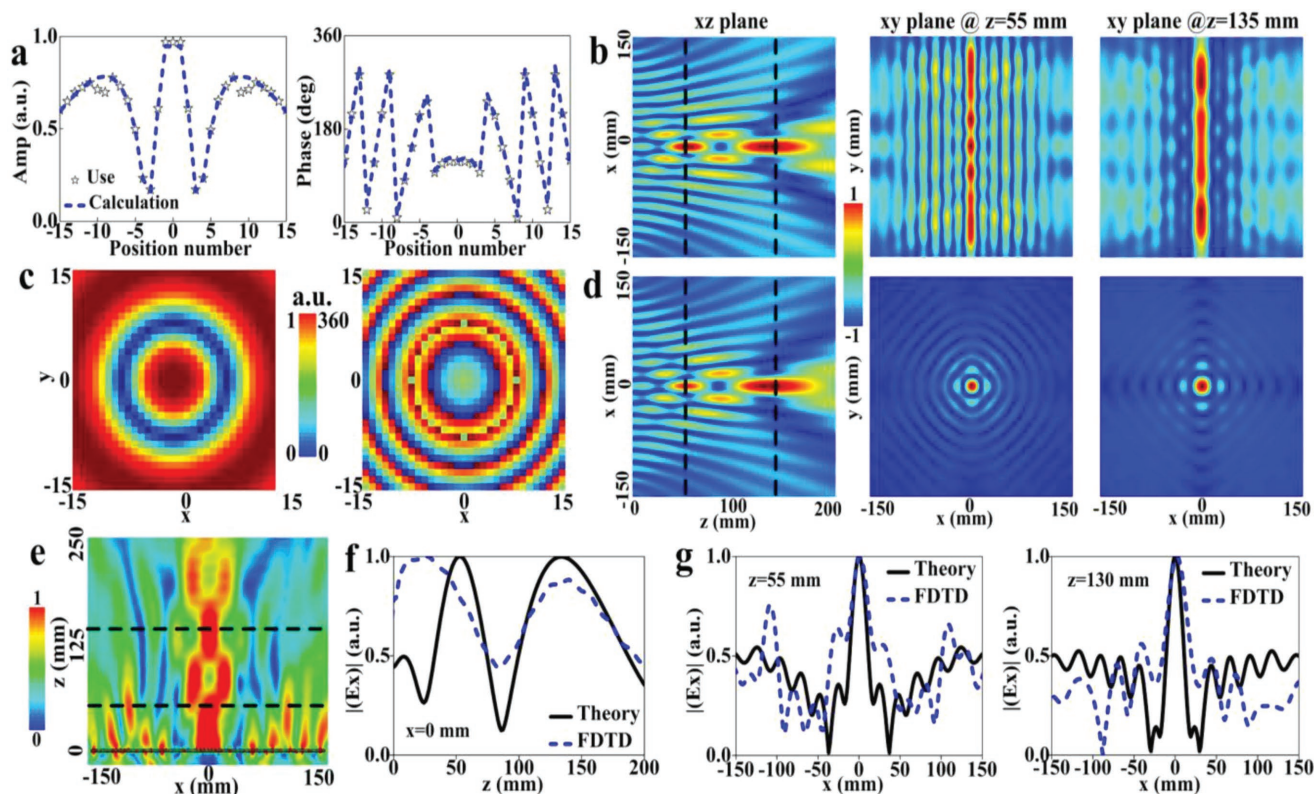


Figure 4. Design, theoretical, and numerical characterizations of the bifocal metalens with axial alignment of two foci at 9.4 GHz. a,c) Required (blue dashed) and digitized (pentacle) amplitudes (left) and phases (right), and b,d) theoretically calculated E-field distributions in the xz- (left) and xy- (right) planes in (a, b) 1D and (c, d) 2D cases. e) FDTD-simulated E_x distributions. g) Comparison of E_x between theoretical and FDTD calculations along f) $x = 0$ mm, g) $z = 55$ mm, and h) $z = 130$ mm. The theoretical near-field distributions evolved along the longitudinal direction are calculated based on Green's functions by imposing homemade codes in a mathematical software.

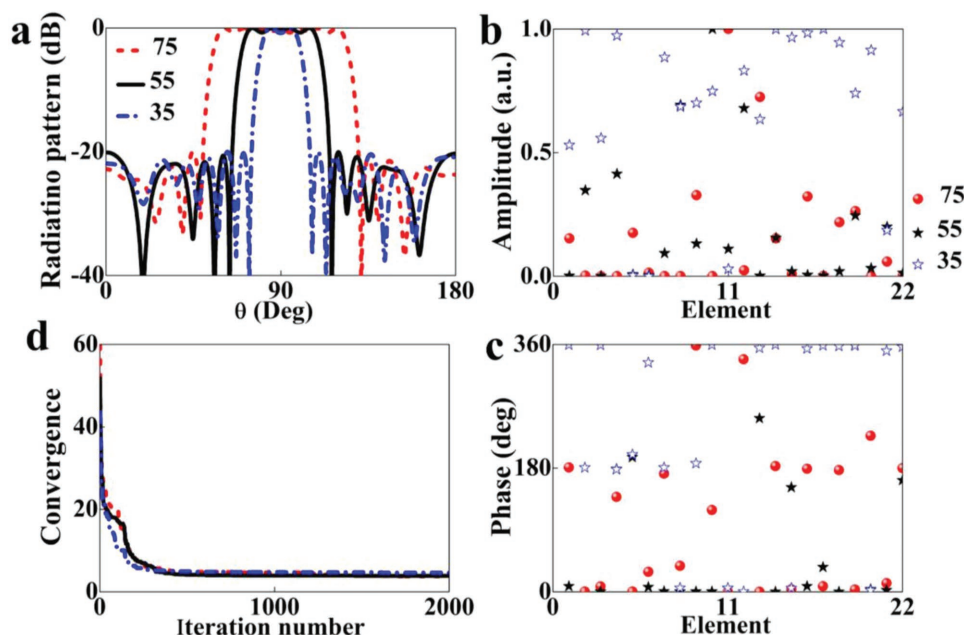


Figure 5. Illustration of possible applications of proposed concept in arbitrary-shaped beam synthesis for different purposes. a) Simulated flat-top scattering patterns with different coverage of 35°, 55°, and 75° in elevation. Optimized b) amplitude and c) phase profile based on genetic algorithms. d) Convergence process as a function of iterations. Here, the metasurface is composed of 22 different meta-atoms with spatially varied R and Φ in the xz-plane, while infinite elements along the y-direction.

can be integrated into one thin plate. Under this frame, we even can envision an incorporation of different shaped patterns of flat-top beam, sector beam, multibeam and cosec-squared patterns, or an integration of a cosecant squared beam in azimuth and a sector beam in elevation.

6. Conclusions

To sum up, we have proposed and demonstrated an efficient approach for simultaneous manipulation of transmissive polarization, amplitude, and phase with high efficiency via theoretical, numerical, and experimental characterizations. By stacking triple-layer SRRs with a specific twist angle, vertical mode magnetoelectric cross-coupling is engineered which thus facilitates complete cross-polarization transmissions within a broad window. Moreover, the independent amplitude and phase modulation is engineered by involving global spatially varied orientations (amplitude) and geometric structures (phase), affording us unprecedented DOF for EM wavefront control. For verification, two metadevices that are impossibly realized through phase-only control of conventional metasurfaces are numerically and experimentally investigated with elegant performances. Our scheme for amplitude and phase decoupling by rotating the meta-atoms can be also observed for large incidence angles and at arbitrary polarizations, thanks to subwavelength 3D chiral architectures, and the simultaneous excitation of symmetric and antisymmetric modes, see Figure S12a–d (Supporting Information). Moreover, it can be even directly extended to circularly polarized operation with a reversed flat magnitude response while a linear phase response as a function of orientations (Figure S12e,f, Supporting Information), revealing a complete decoupling of amplitude, phase, and polarization. We firmly believe our findings significantly expand the capabilities of metasurfaces for arbitrary manipulation of light in a precise and sophisticated manner, and thus promise emerging functional devices and a wide range of EM and photonic applications.

7. Experimental Section

The dual-layer metallic patterns of each metadvice were fabricated individually on two dielectric boards using printed circuit board (PCB) technique. They were first aligned with each other through several embedded vias, assembled together through adhesives, and finally reinforced through a hot press. In near-field (NF) experiments, all measurements were performed in a microwave anechoic chamber to avoid any possible interference from the environment (Figure S11, Supporting Information). The metadvice sample was launched by a LP horn with voltage-standing-wave ratio less than 2 across 8–12 GHz and they were fixed with a distance of 0.7 m. A 15 mm long monopole antenna, functioning as the receiver, was placed behind the sample, and connected to an Agilent N5230C vector network analyzer to record the static EM signals. To guarantee the recorded cross-polarized signal, the monopole was vertically orientated, while the horn was horizontally displaced. Therein, the polarization state between the receiving monopole and the stimulating horn was orthogonal. The monopole was fixed to a 2D electronic step motor that could move automatically in a maximum area of 1.2 m × 1.2 m with a step resolution of 10 mm. Most importantly, the sample was enveloped by a mass of radiation-absorbing materials to avoid possible diffractions from the edge of the sample.

Under this circumstance, the signal emitted from the horn transmits only through the aperture window, while the residual diffractive energy was almost completely blocked.

Supporting Information

Supporting Information is available from the Wiley Online Library or from the author.

Acknowledgements

This work was supported by the National Natural Science Foundation of China (Grant Nos. 61501499, 11634010, 61791082); the Youth Talent Lifting Project of the China Association for Science and Technology (Grant No. 17-JCJQ-QT-003); the National Research Foundation of Singapore (Grant No. NRF-CRP15-2015-03); the Key Program of Natural Science Foundation of Shaanxi Province (Grant No. 2017KJXX-24); the China Scholarship Fund (Grant No. 201703170022); and the Aviation Science Foundation of China (Grant No. 20161996009).

Conflict of Interest

The authors declare no conflict of interest.

Keywords

chirality-assisted metasurface, decoupling, self-accelerating beams, wavefront control

Received: October 29, 2018

Published online:

- [1] N. Yu, P. Genevet, M. A. Kats, F. Aieta, J. P. Tetienne, F. Capasso, Z. Gaburro, *Science* **2011**, 334, 333.
- [2] S. Sun, Q. He, S. Xiao, Q. Xu, X. Li, L. Zhou, *Nat. Mater.* **2012**, 11, 426.
- [3] T. J. Cui, M. Q. Qi, X. Wan, J. Zhao, Q. Cheng, *Light: Sci. Appl.* **2014**, 3, e218.
- [4] H.-X. Xu, L. Zhang, Y. Kim, G.-M. Wang, K.-X. Zhang, Y. Sun, X. Ling, H. Liu, Z. Chen, C.-W. Qiu, *Adv. Opt. Mater.* **2018**, 6, 1800010.
- [5] L. Zhang, S. Liu, L. Li, T. J. Cui, *ACS Appl. Mater. Interfaces* **2017**, 9, 36447.
- [6] M. Q. Mehmood, S. Mei, S. Hussain, K. Huang, S. Y. Siew, L. Zhang, T. Zhang, X. Ling, H. Liu, J. Teng, A. Danner, S. Zhang, C.-W. Qiu, *Adv. Mater.* **2016**, 28, 2533.
- [7] S. M. Kamali, E. Arbabi, A. Arbabi, Y. Horie, M. Faraji-Dana, A. Faraon, *Phys. Rev. X* **2017**, 7, 041056.
- [8] X. Ni, Z. J. Wong, M. Mrejen, Y. Wang, X. Zhang, *Science* **2015**, 349, 1310.
- [9] C. Huang, J. Yang, X. Wu, J. Song, M. Pu, C. Wang, X. Luo, *ACS Photonics* **2018**, 5, 1718.
- [10] Y. Yang, L. Jing, B. Zheng, R. Hao, W. Yin, E. Li, C. M. Soukoulis, H. Chen, *Adv. Mater.* **2016**, 28, 6866.
- [11] F. Qin, L. Ding, L. Zhang, F. Monticone, C. C. Chum, J. Deng, S. Mei, Y. Li, J. Teng, M. Hong, S. Zhang, A. Alù, C.-W. Qiu, *Sci. Adv.* **2016**, 2, e1501168.
- [12] E. Maguid, I. Yulevich, D. Veksler, V. Kleiner, M. L. Brongersma, E. Hasman, *Science* **2016**, 352, 1202.

- [13] H.-X. Xu, S. Tang, C. Sun, L. Li, H. Liu, X. Yang, F. Yuan, Y. Sun, *Photonics Res.* **2018**, 6, 782.
- [14] L. Liu, X. Zhang, M. Kenney, X. Su, N. Xu, C. Ouyang, Y. Shi, J. Han, W. Zhang, S. Zhang, *Adv. Mater.* **2014**, 26, 5031.
- [15] J. Ding, S. An, B. Zheng, H. Zhang, *Adv. Opt. Mater.* **2017**, 5, 1700079.
- [16] Q. Wang, X. Zhang, Y. Xu, J. Gu, Y. Li, Z. Tian, R. Singh, S. Zhang, J. Han, W. Zhang, *Sci. Rep.* **2016**, 6, 32867.
- [17] G. Lee, G. Yoon, S. Lee, H. Yun, J. Cho, K. Lee, H. Kim, J. Rho, B. Lee, *Nanoscale* **2018**, 10, 4237.
- [18] Z. Li, H. Cheng, Z. Liu, S. Chen, J. Tian, *Adv. Opt. Mater.* **2016**, 4, 1230.
- [19] M. Kim, A. M. Wong, G. V. Eleftheriades, *Phys. Rev. X* **2014**, 4, 041042.
- [20] Y. Zhu, J. Hu, X. Fan, J. Yang, B. Liang, X. Zhu, J. Cheng, *Nat. Commun.* **2018**, 9, 1632.
- [21] L. Bao, Q. Ma, G. D. Bai, H. B. Jing, R. Y. Wu, X. Fu, C. Yang, J. Wu, T. J. Cui, *Appl. Phys. Lett.* **2018**, 113, 063502.
- [22] X. Wan, S. L. Jia, T. J. Cui, Y. J. Zhao, *Sci. Rep.* **2016**, 6, 25639.
- [23] G. Minatti, F. Caminita, E. Martini, M. Sabbadini, S. Maci, *IEEE Trans. Antennas Propag.* **2016**, 64, 3907.
- [24] A. Arbabi, Y. Horie, M. Bagheri, A. Faraon, *Nat. Nanotechnol.* **2015**, 10, 937.
- [25] J. P. Balthasar Mueller, N. A. Rubin, R. C. Devlin, B. Groever, F. Capasso, *Phys. Rev. Lett.* **2017**, 118, 113901.
- [26] R. C. Devlin, A. Ambrosio, N.A. Rubin, J. P. B. Mueller, F. Capasso, *Science* **2017**, 358, 896.
- [27] J. Li, S. Chen, H. Yang, J. Li, P. Yu, H. Cheng, C. Gu, H.-T. Chen, *Adv. Funct. Mater.* **2015**, 25, 704.
- [28] H.-X. Xu, S. Tang, G.-M. Wang, T. Cai, W. Huang, Q. He, S. Sun, L. Zhou, *IEEE Trans. Antennas Propag.* **2016**, 64, 3676.
- [29] P. C. Wu, W.-Y. Tsai, W. T. Chen, Y.-W. Huang, T.-Y. Chen, J.-W. Chen, C. Y. Liao, C. H. Chu, G. Sun, D. P. Tsai, *Nano Lett.* **2017**, 17, 445.
- [30] H.-X. Xu, S. Tang, S. Ma, W. Luo, T. Cai, S. Sun, Q. He, L. Zhou, *Sci. Rep.* **2016**, 6, 38255.
- [31] W. Luo, S. Xiao, Q. He, S. Sun, L. Zhou, *Adv. Opt. Mater.* **2015**, 3, 1102.
- [32] G. Zheng, H. Muhlenbernd, M. Kenney, G. Li, T. Zentgraf, S. Zhang, *Nat. Nanotechnol.* **2015**, 10, 308.
- [33] H.-X. Xu, S. Ma, X. Ling, X.-K. Zhang, S. Tang, T. Cai, S. Sun, Q. He, L. Zhou, *ACS Photonics* **2018**, 5, 1691.
- [34] C. Pfeiffer, A. Grbic, *Phys. Rev. Lett.* **2013**, 110, 197401.
- [35] C. Pfeiffer, N. K. Emani, A. M. Shaltout, A. Boltasseva, V. M. Shalaev, A. Grbic, *Nano Lett.* **2014**, 14, 2491.
- [36] W. Luo, S. Sun, H.-X. Xu, Q. He, L. Zhou, *Phys. Rev. Appl.* **2017**, 7, 044033.
- [37] X. Ding, F. Monticone, K. Zhang, L. Zhang, D. Gao, S. N. Burokur, A. de Lustrac, Q. Wu, C.-W. Qiu, A. Alù, *Adv. Mater.* **2015**, 27, 1195.
- [38] D. Lin, P. Fan, E. Hasman, M. L. Brongersma, *Science* **2014**, 345, 298.
- [39] Q.-T. Li, F. Dong, B. Wang, F. Gan, J. Chen, Z. Song, L. Xu, W. Chu, Y.-F. Xiao, Q. Gong, Y. Li, *Opt. Express* **2016**, 24, 16309.
- [40] Y. Zhao, M.A. Belkin, A. Alù, *Nat. Commun.* **2012**, 3, 870.
- [41] J. Durnin, J. J. Miceli, J. H. Eberly, *Phys. Rev. Lett.* **1987**, 58, 1499.
- [42] M. V. Berry, N. L. Balazs, *Am. J. Phys.* **1979**, 47, 264.
- [43] G. A. Siviloglou, J. Broky, A. Dogariu, D. N. Christodoulides, *Phys. Rev. Lett.* **2007**, 99, 213901.